Axial-mode solid-state thermoacoustic instability: An analytical parametric study

Haitian Hao [a,b], Carlo Scalo [a], Fabio Semperlotti [a,b,*]

[a] School of Mechanical Engineering, Purdue University, West Lafayette, IN 47907, USA
[b] Ray W. Herrick Laboratories, 177 South Russell Street, West Lafayette, IN 47907, USA

ARTICLE INFO

ABSTRACT

Solid-state thermoacoustic (SSTA) instability refers to the occurrence of unstable thermoelastic oscillations of solid media when in presence of a spatial temperature gradient. Recently, theoretical and numerical studies have shown that both standing and traveling thermoacoustic waves can exist in solids. The many mechanisms available in solids to tailor either their physical or effective properties offer remarkable opportunities to enhance and tune the performance of SSTA devices. A thorough understanding of the functional relationships controlling the complex dynamics in solid-state thermoacoustics (SSTAs) is critical to design efficient SSTA machines. In this paper, we first recast the governing equations of SSTAs into dimensionless form; then, we develop accurate analytical approaches to solve for the mode shapes and complex frequencies for 1) a standing-wave fixed-mass SSTA rod, and 2) for a traveling-wave looped SSTA rod. It is found that the growth-rate-to-frequency ratio is governed by the dimensionless coefficient of thermal expansion (CTE), the Grüneisen parameter, the hot-to-cold temperature ratio, the normalized stage location and length, the dimensionless radius, the end mass ratio for the fixed-mass rod, and the thermal buffer segment (TBS) length for the looped rod. Based on these newly identified dimensionless parameters a thorough numerical analysis is conducted in order to shed light on the optimal design of SSTA devices.

© 2019 Elsevier Ltd. All rights reserved.

1. Introduction

Thermoacoustic (TA) instability is a well-known phenomenon commonly seen in fluids. When driven by combustion [1], TA instability is harmful to the structural and operational integrity of the system. However, the intrinsic energy conversion mechanism at the basis of TA oscillations [2] inspired the design of thermoacoustic engines (TAEs) and refrigerators (TARs) where the instability is not only desired, but maximized when possible [3–5]. A simple example of TAE is the Rijke's tube [6] which amplifies acoustic waves via wall heat transfer. In both cases, the mutual interaction of velocity and heat release rate fluctuation is established, effectively converting the heat energy into mechanical (acoustic) energy. The inverse mechanism takes place in TARs. For practical applications, piezoelectric elements can be integrated with TAEs to accomplish an additional mechanical-to-electrical energy conversion process [7]. The theoretical foundation of TA instability was laid by Rott in 1969 [8]. Only recently, the theory of TA oscillations in solids, namely solid-state thermoacoustics (SSTA), was established in Ref. [9]. This study showed the existence of self-sustained standing-wave TA oscillations, as well as traveling wave modes, capable of a more efficient conversion of heat into mechanical energy [10].

---

* Corresponding author. School of Mechanical Engineering, Purdue University, West Lafayette, IN 47907, USA.
E-mail addresses: haoh@purdue.edu (H. Hao), scalo@purdue.edu (C. Scalo), fsemperl@purdue.edu (F. Semperlotti).

Solids offer unique opportunities to tailor both physical and effective dynamic properties that can ultimately greatly benefit the thermoacoustic response of SSTA. The many recent efforts in the development of engineered materials and structures have highlighted the remarkable design space offered by these man-made materials. [11,12] In order to take full advantage of this capability of tailoring the dynamic response of solids for the design of SSTA devices methodologies for the systematic performance and parametric analysis of SSTA systems are necessary.

In this study, we propose an analytical approach to solve the governing equations of axial-mode standing and traveling SSTA waves in a fixed-mass rod [9] and a looped rod [10] configuration, respectively. The governing equations are recast into dimensionless form facilitating the identification of a set of seven dimensionless parameters that directly impact the growth-rate-to-frequency ratio (growth ratio) [13]. In the present study, this ratio is considered as the fundamental metric to compare the performance of different designs. The seven dimensionless parameters are: the dimensionless coefficient of thermal expansion (CTE), the Grüneisen parameter, the hot-to-cold temperature ratio, the normalized stage location and length, the dimensionless radius, the end mass ratio for the fixed-mass rod, and the dimensionless thermal buffer segment (TBS) length for the looped rod. The above parameters will be analyzed in detail particularly from a perspective of growth ratio optimization. This parametric analysis allows shedding light on the effect of different material and structural parameters on the design of SSTA devices.

2. Mathematical model

2.1. Dimensional equations

The two configurations being considered in this study are: 1) the fixed-mass axial SSTA [9], and 2) the looped rod in Ref. [10]. The axial thermoacoustic modes for both systems can be obtained using the following governing equations:

$$i\Lambda\widehat{u} = \widehat{v} \tag{1}$$

$$i\Lambda\widehat{v} = \frac{E}{\rho}\left(\frac{\mathrm{d}^2\widehat{u}}{\mathrm{d}x^2} - \alpha\frac{\mathrm{d}\widehat{T}}{\mathrm{d}x}\right) \tag{2}$$

$$i\Lambda\widehat{T} = -\frac{\mathrm{d}T_0(x)}{\mathrm{d}x}\widehat{v} + i\Lambda G_k(x)\widehat{T} - \gamma_G T_0(x)\frac{\mathrm{d}\widehat{v}}{\mathrm{d}x} \tag{3}$$

where E is the Young's modulus, ρ is the material density, α is the coefficient of thermal expansion (CTE), $\gamma_G = \alpha E/(\rho c_\varepsilon)$ is the 1D Grüneisen parameter [14], c_ε is the specific heat at constant strain, L is the rod length, $i\Lambda = B + i\Omega$ is the generic eigenvalue where B is the growth rate and Ω is the angular frequency.

The two SSTA configurations differ in terms of the distribution of the reference mean temperature $T_0(x)$, function $G_k(x)$ and of the boundary conditions (BCs). The specific conditions for the two cases are given here below:

Case 1: Fixed-mass rod - Standing mode SSTA

$$T_0(x) = \begin{cases} T_h & 0 < x < x_h \\ T_h + \dfrac{T_c - T_h}{x_c - x_h}(x - x_h) & x_h < x < x_c \\ T_c & x_c < x < L \end{cases} \tag{4}$$

$$G_k(x) = \begin{cases} g_k = \dfrac{1}{1 - \frac{1}{2}\zeta_{top}\frac{J_0(\zeta_{top})}{J_1(\zeta_{top})}} & x_h < x < x_c \\ 0 & \text{elsewhere} \end{cases}, \tag{5}$$

where x_h and x_c are the axial locations of the two ends of the stage, T_h and T_c are temperatures of segment 1 ($0 < x < x_h$) and segment 3 ($x_c < x < L$), corresponding to the hot and cold temperatures. $G_k(x)$ is a dimensionless piecewise-constant function of the coordinate x [15], $J_n(\cdot)$ are Bessel functions of the first kind, and ζ_{top} is given by:

$$\zeta_{top} = \sqrt{-2i}\frac{R}{\delta_k} \tag{6}$$

where R is the bar radius, $\delta_k = \sqrt{2\kappa/(\Omega\rho c_\varepsilon)}$ is the thermal penetration depth depending on the frequency Ω, and κ is the thermal conductivity.

The dimensional boundary conditions are:

$$\widehat{u}|_{x=0} = 0 \tag{7}$$

$$\widehat{\sigma}|_{x=L}\mathcal{A} = -i\Lambda(\widehat{v}|_{x=L})M \tag{8}$$

Table 1
Dimensionless variables, parameters, and auxiliary dimensional quantities.

Dimensionless variables	
$\xi = x/L$	Dimensionless axial coordinate
$u = \hat{u}/L$	Dimensionless particle displacement
$v = \hat{v}/a_0$	Dimensionless particle velocity
$T = \hat{T}/T_c$	Dimensionless temperature fluctuation
$\sigma = \hat{\sigma}/E = du/d\xi - AT$	Dimensionless stress
$i\lambda = i\Lambda/\omega_0$	Dimensionless eigenvalue
$\beta = B/\omega_0$	Dimensionless growth rate
$\omega = \Omega/\omega_0$	Dimensionless angular frequency
Dimensionless parameters	
$A = \alpha T_c$	Dimensionless coefficient of thermal expansion (CTE)
$\gamma_G = \alpha E/(\rho c_\varepsilon)$	Grüneisen constant
$\Theta = T_h/T_c$	Temperature ratio
$r = R/\delta_k$	Dimensionless radius (frequency dependent)
$\xi_h = x_h/L$	Dimensionless stage hot end position
$\xi_c = x_c/L$	Dimensionless stage cold end position
$\xi_b = x_b/L$	Dimensionless TBS end position (looped rod only)
$m = M/(\rho L \mathcal{A})$	Mass ratio (fixed-mass rod only)
Auxiliary dimensional quantities	
$a_0 = \sqrt{E/\rho}\ [\text{m/s}]$	Sound speed
$\omega_0 = a_0/L\ [1/\text{s}]$	Characteristic frequency
$\delta_k = \sqrt{2\kappa/(\Omega \rho c_\varepsilon)}\ [\text{m}]$	Thermal penetration depth (frequency-dependent)

where $\mathcal{A}$ is the rod cross-sectional area, and M is the end mass.

Case 2: Looped rod - Traveling mode SSTA

$$T_0(x) = \begin{cases} T_c & 0 < x < x_c,\ x_b < x < L \\ T_c + \dfrac{T_h - T_c}{x_h - x_c}(x - x_c) & x_c < x < x_h \\ T_h + \dfrac{T_b - T_h}{x_b - x_h}(x - x_h) & x_h < x < x_b \end{cases} \tag{9}$$

$$G_k(x) = \begin{cases} g_k & x_c < x < x_h \\ 0 & \text{elsewhere} \end{cases}, \tag{10}$$

where x_b is the end position of the thermal buffer segment (TBS).

The dimensional BCs are:

$$\hat{u}|_{x=0} = \hat{u}|_{x=L} \tag{11}$$

$$\hat{\sigma}|_{x=0} = \hat{\sigma}|_{x=L} \tag{12}$$

2.2. Dimensionless equations

Considering Table 1, we can recast both the governing equations (1)–(3) and the boundary conditions (7–12) into a dimensionless form:

$$i\lambda u = v \tag{13}$$

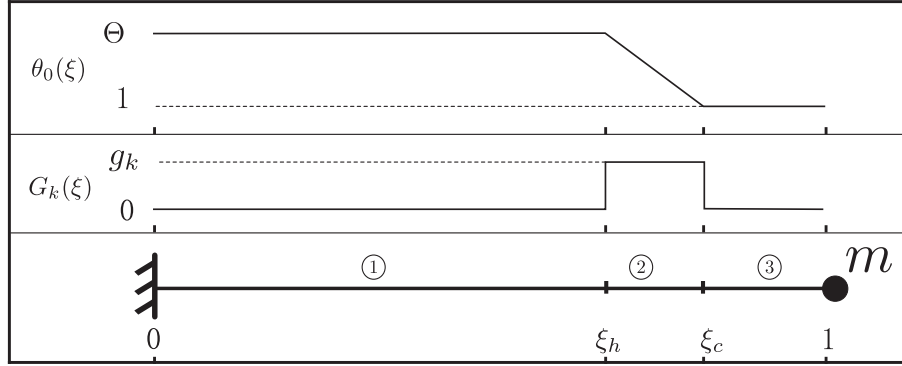$$i\lambda v = \frac{d^2 u}{d\xi^2} - A\frac{dT}{d\xi} \tag{14}$$

$$i\lambda T = -\frac{d\theta_0(\xi)}{d\xi}v - \gamma_G \theta_0(\xi)\frac{dv}{d\xi} + i\lambda G_k(\xi)T \tag{15}$$

Fixed-mass:

$$u|_{\xi=0} = 0 \tag{16}$$

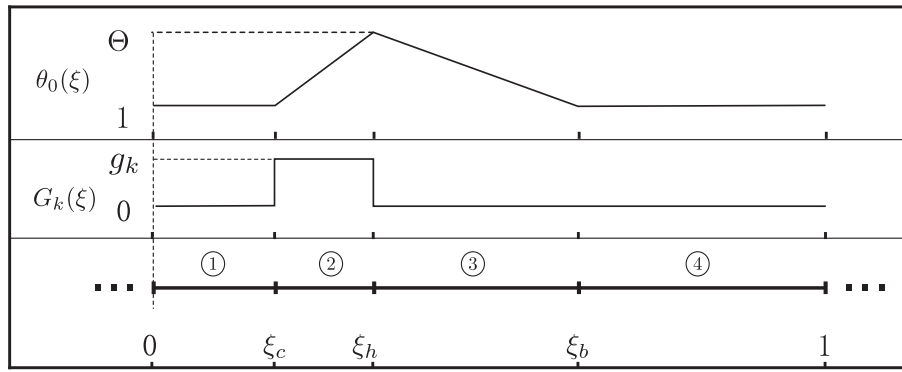$$\sigma|_{\xi=1} = m\lambda^2 u|_{\xi=1} \tag{17}$$

Fig. 1. Distribution of $\theta_0(\xi)$ and $G_k(\xi)$ for the fixed-mass rod and the looped rod. Circled numbers indicate the segmentation of the rods.

Looped:

$$u|_{\xi=0} = u|_{\xi=L} \tag{18}$$

$$\sigma|_{\xi=0} = \sigma|_{\xi=L} \tag{19}$$

Fig. 1 shows the distribution of the dimensionless mean temperature $\theta_0(\xi)$ and of the wall-heat-transfer function $G_k(\xi)$.

3. Derivation and validation of the analytical approach

From Eqns. (13)–(19), the dimensionless parameters which determine the value of λ are the material parameters A and γ_G, the dimensionless temperature profile $\theta_0(\xi)$, specifically Θ, ξ_h and ξ_c, the frequency-dependent dimensionless radius r, which determines g_k, and (only for the fixed-mass case) the mass ratio m.

Rearranging Eqn. (15), a local solution of T is obtained:

$$T = \frac{[\mathrm{d}\theta_0(\xi)/\mathrm{d}\xi]u + \gamma_G\theta_0(\xi)[\mathrm{d}u/\mathrm{d}\xi]}{G_k(\xi) - 1} \tag{20}$$

Thus:

$$\frac{\mathrm{d}T}{\mathrm{d}\xi} = (G_k(\xi) - 1)^{-1}[(1 + \gamma_G)\frac{\mathrm{d}\theta_0}{\mathrm{d}\xi}\frac{\mathrm{d}u}{\mathrm{d}\xi} + \gamma_G\theta_0(\xi)\frac{\mathrm{d}^2u}{\mathrm{d}\xi^2}] \tag{21}$$

Note that $\mathrm{d}^2\theta_0/\mathrm{d}\xi^2 = 0$ is assumed due to the piece-wise linearity of $\theta_0(\xi)$.

Substituting Eqns. (13) and (21) into Eqn. (14) and rearranging, a second order ODE is obtained:

$$a(\xi)\frac{\mathrm{d}^2u}{\mathrm{d}\xi^2} + b(\xi)\frac{\mathrm{d}u}{\mathrm{d}\xi} + cu = 0 \tag{22}$$

where:

$$a(\xi) = 1 + \frac{A\gamma_G}{1 - G(x)}\theta_0(\xi) \tag{23}$$

Table 2
Coefficients $a(\xi)$, $b(\xi)$, and c for segments of the fixed-mass rod.

Segment 1 ($0 < \xi < \xi_h$):	$\begin{cases} a_1 &= 1 + A\gamma_G\Theta \\ b_1 &= 0 \\ c_1 &= \lambda^2 \end{cases}$
Segment 2 ($\xi_h < \xi < \xi_c$):	$\begin{cases} a_2(\xi) &= 1 + \dfrac{A\gamma_G}{1-g_k}(\Theta + \dfrac{1-\Theta}{\xi_c-\xi_h}(\xi-\xi_h)) \\ b_2 &= \dfrac{A(1+\gamma_G)}{1-g_k}\dfrac{1-\Theta}{\xi_c-\xi_h} \\ c_2 &= \lambda^2 \end{cases}$
Segment 3 ($\xi_c < \xi < 1$):	$\begin{cases} a_3 &= 1 + A\gamma_G \\ b_3 &= 0 \\ c_3 &= \lambda^2 \end{cases}$

$$b(\xi) = \frac{A(1+\gamma_G)}{1-G(x)}\frac{\mathrm{d}\theta_0(\xi)}{\mathrm{d}\xi} \tag{24}$$

$$C = \lambda^2 \tag{25}$$

From this point on, the procedure for the two cases requires a different treatment.

Case 1: Fixed-mass rod (Standing mode):

For the three segments shown in Fig. 1 (1: $0 < \xi < \xi_h$, 2: $\xi_h < \xi < \xi_c$, 3: $\xi_c < \xi < 1$), the expressions for $a(\xi)$, $b(\xi)$, and c are given in Table 2.

So for Segment 1 and 3, Eqn. (22) degenerates to two constant-coefficient second order ODEs. Their general solution is given by:

$$u_1 = A_1 e^{i\lambda R_1\xi} + B_1 e^{-i\lambda R_1\xi} \tag{26}$$

$$u_3 = A_3 e^{i\lambda R_3\xi} + B_3 e^{-i\lambda R_3\xi} \tag{27}$$

where A_1, B_1, A_3, and B_3 are coefficients to be determined, while R_1 and R_3 are given by:

$$R_1 = \frac{1}{\sqrt{1+A\gamma_G\Theta}} \tag{28}$$

$$R_3 = \frac{1}{\sqrt{1+A\gamma_G}} \tag{29}$$

For Segment 2, $a(\xi)$ becomes a linear function $a_2(\xi) = a_{21} + a_{22}\xi$ where:

$$a_{21} = 1 + \frac{A\gamma_G}{1-g_k}\left(\Theta - \frac{1-\Theta}{\xi_c-\xi_h}\xi_h\right) \tag{30}$$

$$a_{22} = \frac{A\gamma_G}{1-g_k}\left(\frac{1-\Theta}{\xi_c-\xi_h}\right) \tag{31}$$

and $b(\xi)$ becomes a constant b_2 (Table 2). Thus Eqn. (22) for this segment becomes:

$$(a_{21} + a_{22}\xi)\frac{\mathrm{d}^2u_2}{\mathrm{d}\xi^2} + b_2\frac{\mathrm{d}u_2}{\mathrm{d}\xi} + c_2 u_2 = 0 \tag{32}$$

Assume that the solution u_2 can be expanded via a Taylor series that converges on the interval ($\xi_h < \xi < \xi_c$). Specifically:

$$u_2 = \sum_{n=0}^{\infty} \beta_n \xi^n \tag{33}$$

Substituting the expansion back into Eqn. (32) yields:

$$\sum_{n=1}^{\infty}\left[a_{21}(n+2)(n+1)\beta_{n+2} + [b_2 + a_{22}n](n+1)\beta_{n+1} + c_2\beta_n\right]\xi^n$$

$$+ \left[2a_{21}\beta_2 + b_2\beta_1 + c_2\beta_0\right] = 0 \tag{34}$$

Considering that ξ^j is independent of ξ^k for $j \neq k$, for any $n \geqslant 0$, the above equation gives:

$$a_{21}(n + 2)(n + 1)\beta_{n+2} + [b_2 + a_{22}n](n + 1)\beta_{n+1} + c_2\beta_n = 0 \tag{35}$$

From Eqn. (35), all β_n for $n \geqslant 2$ could be determined from assigned values of β_0 and β_1. β_n can be expressed as a linear combination of β_0 and β_1, namely:

$$\beta_n = c_{\beta 0}(n)\beta_0 + c_{\beta 1}(n)\beta_1 \qquad n \geqslant 2 \tag{36}$$

where, the coefficients $c_{\beta 0}(n)$ and $c_{\beta 1}(n)$ can be found recursively by:

$$c_{\beta 0}(n + 2) = -\frac{c_2}{a_{21}(n + 2)(n + 1)}c_{\beta 0}(n) - \frac{b_2 + a_{22}n}{a_{21}(n + 2)}c_{\beta 0}(n + 1) \tag{37}$$

$$c_{\beta 1}(n + 2) = -\frac{c_2}{a_{21}(n + 2)(n + 1)}c_{\beta 1}(n) - \frac{b_2 + a_{22}n}{a_{21}(n + 2)}c_{\beta 1}(n + 1), \qquad n \geqslant 0 \tag{38}$$

$$c_{\beta 0}(0) = 1, \quad c_{\beta 0}(1) = 0, \quad c_{\beta 1}(0) = 0, \quad c_{\beta 1}(1) = 1 \tag{39}$$

Consider the fact that Eqns. (13)–(17) are linear equations; and u, v, and T denote the corresponding mode shapes, A_1 is arbitrarily taken as $A_1 = 1$. Therefore, the six independent unknowns $\beta_0, \beta_1, B_1, B_2, B_3$ and λ should be evaluated. The boundary conditions of each segment (a total of six BCs) are expressed as:

$$\xi = 0: \quad u_1|_{\xi=0} = 0 \tag{40}$$

$$\xi = \xi_h: \quad u_1|_{\xi=\xi_h} = u_2|_{\xi=\xi_h} \tag{41}$$

$$\xi = \xi_h: \quad \sigma_1|_{\xi=\xi_h} = \sigma_2|_{\xi=\xi_h} \tag{42}$$

$$\xi = \xi_c: \quad u_2\Big|_{\xi=\xi_c} = u_3\Big|_{\xi=\xi_c} \tag{43}$$

$$\xi = \xi_c: \quad \sigma_2\Big|_{\xi=\xi_c} = \sigma_3\Big|_{\xi=\xi_c} \tag{44}$$

$$\xi = 1: \quad \sigma_3|_{\xi=1} = m\lambda^2(u_3|_{\xi=1}) \tag{45}$$

This set of equations could be solved iteratively by initializing the calculation with an initial guess $\lambda^{(0)}$. The steps of one iteration are as follows:

Step 1: By Eqn. (40):

$$B_1 = -1 \tag{46}$$

$$u_1 = 2i\sin(\lambda R_1\xi) \tag{47}$$

Step 2: Eqns. (41) and (42) give:

$$\underline{F}_2 = \underline{C}_2\,\underline{b}_2 \tag{48}$$

where:

$$\underline{F}_2 = 2\mathbf{i}\begin{bmatrix} 1 & 0 \\ -\dfrac{A}{1 - g_k}\dfrac{1 - \Theta}{\xi_h - \xi_c} & (1 + A\gamma_G\Theta)(\lambda R_1) \end{bmatrix}\begin{bmatrix} \sin\left(\lambda R_1\xi_h\right) \\ \cos\left(\lambda R_1\xi_h\right) \end{bmatrix} \tag{49}$$

$$\underline{C}_2 = \begin{bmatrix} 1 + \displaystyle\sum_{n=2}^{\infty}\xi_h^n c_{\beta 0}(n) & \xi_h + \displaystyle\sum_{n=2}^{\infty}\xi_h^n c_{\beta 1}(n) \\ \left(1 + \dfrac{A\gamma_G\Theta}{1 - g_k}\right)\displaystyle\sum_{n=2}^{\infty}n\xi_h^{n-1}c_{\beta 0}(n) & \left(1 + \dfrac{A\gamma_G\Theta}{1 - g_k}\right)\left(1 + \displaystyle\sum_{n=2}^{\infty}n\xi_h^{n-1}c_{\beta 1}(n)\right) \end{bmatrix} \tag{50}$$

$$\underline{b}_2 = \begin{bmatrix} \beta_0 \\ \beta_1 \end{bmatrix} \tag{51}$$

Rename β_0 and β_1 as A_2 and B_2. They are therefore given by:

$$\begin{bmatrix} A_2 \\ B_2 \end{bmatrix} = \underline{b}_2 = \underline{C}_2^{-1}\underline{F}_2 \tag{52}$$

Table 3
Coefficients $a(\xi)$, $b(\xi)$, and c for segments of the looped rod.

Segment 1 & 4 $(0 < \xi < \xi_c, \xi_b\xi < 1)$:	$\begin{cases} a_{1,4} & = 1 + A\gamma_G \\ b_{1,4} & = 0 \\ c_{1,4} & = \lambda^2 \end{cases}$
Segment 2 $(\xi_h < \xi < \xi_c)$:	$\begin{cases} a_2(\xi) & = 1 + \dfrac{A\gamma_G}{1 - g_k}(1 + \dfrac{1 - \Theta}{\xi_c - \xi_h}(\xi - \xi_c)) \\ b_2 & = \dfrac{A(1 + \gamma_G)}{1 - g_k}\dfrac{1 - \Theta}{\xi_c - \xi_h} \\ c_2 & = \lambda^2 \end{cases}$
Segment 3 $(\xi_c < \xi < 1)$:	$\begin{cases} a_2(\xi) & = 1 + (A\gamma_G)(\Theta + \dfrac{1 - \Theta}{\xi_b - \xi_h}(\xi - \xi_h)) \\ b_2 & = A(1 + \gamma_G)\dfrac{1 - \Theta}{\xi_b - \xi_h} \\ c_2 & = \lambda^2 \end{cases}$

Step 3: Eqns. (43) and (44) give:

$$\underline{F}_3 = \underline{C}_3\,\underline{b}_3 \tag{53}$$

where:

$$\underline{F}_3 = \begin{bmatrix} 0 & 1 \\ 1 + \dfrac{A\gamma_G}{1 - g_k} & \dfrac{A}{1 - g_k}\dfrac{1 - \Theta}{\xi_c - \xi_h} \end{bmatrix} \begin{bmatrix} \sum_{n=1}^{\infty} \beta_n n\xi_c^{n-1} \\ \sum_{n=0}^{\infty} \beta_n\xi_c^n \end{bmatrix} \tag{54}$$

$$\underline{C}_3 = \begin{bmatrix} \exp(\mathrm{i}\lambda R_3\xi_c) & \exp(-\mathrm{i}\lambda R_3\xi_c) \\ \left[1 + A\gamma_G(2\mathrm{i}\lambda R_3)\right]\exp\left(\mathrm{i}\lambda R_3\xi_c\right) & -\left[1 + A\gamma_G(2\mathrm{i}\lambda R_3)\right]\exp\left(\mathrm{i}\lambda R_3\xi_c\right) \end{bmatrix} \tag{55}$$

$$\underline{b}_3 = \begin{bmatrix} A_3 \\ B_3 \end{bmatrix} \tag{56}$$

Therefore, A_3 and B_3 are given by:

$$\begin{bmatrix} A_3 \\ B_3 \end{bmatrix} = \underline{b}_3 = \underline{C}_3^{-1}\underline{F}_3 \tag{57}$$

Step 4: By Eqn. (45), λ can be solved iteratively through:

$$\lambda^{(p+1)} = \mathrm{i}\frac{\left(1 + A\gamma_G\right)R_3}{m}\frac{A_3\exp\left(\mathrm{i}\lambda^{(p)}R_3\right) - B_3\exp\left(-\mathrm{i}\lambda^{(p)}R_3\right)}{A_3\exp\left(\mathrm{i}\lambda^{(p)}R_3\right) + B_3\exp\left(-\mathrm{i}\lambda^{(p)}R_3\right)} \tag{58}$$

where (p) is the index for iterative step.

Step 5: Average $\lambda^{(p+1)}$ and $\lambda^{(p)}$, and perform a new iteration until the difference between λ's from two consecutive iterations is satisfied.

The coefficients A_j and B_j, $(j = 1, 2, 3)$ are expressed by Eqns. (46), (52) and (57) once λ reaches its convergence value. Thus, the displacement mode shape u_j, the strain $\varepsilon_j = \mathrm{d}u_j/\mathrm{d}\xi$, and the temperature T_j (see Eqn. (20)) for the three segments can be written in terms of A_j, B_j, and λ.

Case 2: Looped rod (Traveling mode)

The looped rod is virtually divided into four segments (Fig. 1), while continuity conditions (continuous u and σ) hold at $\xi_h\xi_c$ and ξ_b. In this case, The quantities $a(\xi)$, $b(\xi)$, and c are given in Table 3.

By the periodicity condition at $\xi = 0$ and $\xi = 1$, the displacement u of Segment 1 and 4 are:

$$u_1 = A_1\mathrm{e}^{\mathrm{i}\lambda R_3\xi} + B_1\mathrm{e}^{-\mathrm{i}\lambda R_3\xi} \tag{59}$$

$$u_4 = A_1\mathrm{e}^{\mathrm{i}\lambda R_3(\xi-1)} + B_1\mathrm{e}^{-\mathrm{i}\lambda R_3(\xi-1)} \tag{60}$$

Assuming that the displacement of Segment 2 and 3, (i.e. u_2 and u_3) have converging Taylor series on their own intervals:

$$u_2 = \sum_{n=0}^{\infty} \varphi_n\xi^n \tag{61}$$

Table 4
Dimensional parameters used in numerical simulations.

General:			
$\alpha = 23 \times 10^{-6}$ [1/K]	$E = 70$ [GPa]	$\rho = 2700$ [kg/m^3]	$\kappa = 238$ [W/mK]
$c_\varepsilon = 900$ [J/kgK]	$T_h = 493.15$ [K]	$T_c = 293.15$ [K]	$L = 1.8$ [m]
Fixed-mass rod:			
$x_h = 0.9L$	$x_c = 0.95L$	$r = 1$ [mm]	$M = 0.3527$ [kg]
Looped rod:			
$x_c = 0.18L$	$x_h = 0.23L$	$x_b = 0.68L$	$r = 0.1$ [mm]

Table 5
Dimensionless parameters used in analytical approach.

General:	$A = 6.74 \times 10^{-3}$	$\gamma_G = 0.6626$	$\Theta = 1.682$	
Fixed-mass rod:	$r = 3.80\sqrt{1/\omega}$	$\xi_h = 0.9$	$\xi_c = 0.95$	$m = 23.101$
Looped rod:	$r = 0.38\sqrt{1/\omega}$	$\xi_c = 0.18$	$\xi_h = 0.23$	$\xi_b = 0.68$

$$u_3 = \sum_{n=0}^{\infty} \psi_n \xi^n \tag{62}$$

Similar to Case 1, φ_n and ψ_n are linear combinations of φ_0 and φ_1, and ψ_0 and ψ_1, respectively:

$$\varphi_n = d_{\varphi 0}(n)\varphi_0 + d_{\varphi 1}(n)\varphi_1 \qquad n \geqslant 2 \tag{63}$$

$$\psi_n = d_{\psi 0}(n)\psi_0 + d_{\psi 1}(n)\psi_1 \qquad n \geqslant 2 \tag{64}$$

where the coefficients $d_{\varphi 0}(n)$, $d_{\varphi 1}(n)$, $d_{\psi 0}(n)$, and $d_{\psi 1}(n)$ can be found recursively in the same fashion described in Case 1 (see Eqns. (37) and (38)). By applying the continuity conditions at ξ_c, ξ_h, and ξ_b the following equation holds:

$$\underline{C}\,\underline{b} = 0 \tag{65}$$

where $\underline{C}$ is a 6 $\times$ 6 matrix whose elements are given in Appendix A. The vector $\underline{b}$ is:

$$\underline{b} = \left[A_1\ B_1\ \varphi_0\ \varphi_1\ \psi_1\ \psi_1 \right]^{\text{T}} \tag{66}$$

From Eqn. (65), the complex frequency λ is the root of:

$$\det[\underline{C}(\lambda)] = 0 \tag{67}$$

which can be solved by a nonlinear numerical root finding approach. By arbitrarily choosing $A_1 = 1$, the remaining elements in the vector $\underline{b}$ can be calculated. These coefficients enable recovering the mode shapes of displacement, strain and temperature.

To validate the analytical approach, we performed numerical simulations using the dimensional parameters tabulated in Table 4.The dimensional parameters were used in the numerical solver adopted by Ref. [9]. The spatial domain was discretized uniformly into 500 cells using a central Euler scheme on a staggered grid. The output eigenvalue and mode shape will be reported later in comparison to the analytical results.

The dimensional parameters can be grouped and recast into dimensionless parameters (Table 5).

Note that r is a frequency dependent quantity, which can be determined in either the iterative process or the nonlinear root finder.

λ is then solved differently for the two cases:

Fixed-mass rod: To solve for λ, Eqn. (33) was truncated to six terms. By Eqn. (58), the value of λ at convergence was calculated as $0.20714 - (1.5215 \times 10^{-4})$i. The iteration of the real and imaginary parts of λ are shown in Fig. 2. It is seen that the iterative process is very efficient for the calculation of λ. The dimensional eigenvalue iΛ can be recovered as $0.430 + 585.95$i, the error is within 0.5% from $0.429 + 584.68$i, the result calculated by the numerical solver with $N = 500$ cells.

Looped rod: Equation (67) is divided into real and imaginary parts and numerically solved for Re[λ] and Im[λ]. λ is returned as 6.2984–1.7598i. The dimensional eigenvalue iΛ can be recovered as $4.9781 + 17816.51$i which has an error within 1% from the numerical solution $4.9209 + 17816.32$i obtained using $N = 500$ cells.

The amplitude normalized mode shapes for displacement $\overline{u}$, strain $\overline{\varepsilon}$, and temperature fluctuation $\overline{T}$ are shown in Fig. 3, where $\overline{z} = |z|/\max(|z|)$, and $z = u, \varepsilon$ or T. The good agreement between the results provide good confidence in the validity of the analytical approaches.
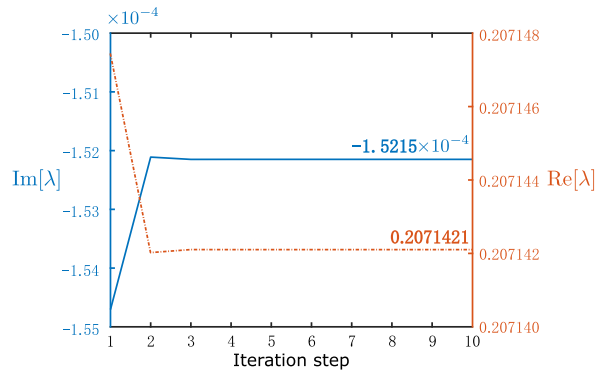
Fig. 2. Iteration of real and imaginary part of the dimensionless λ.
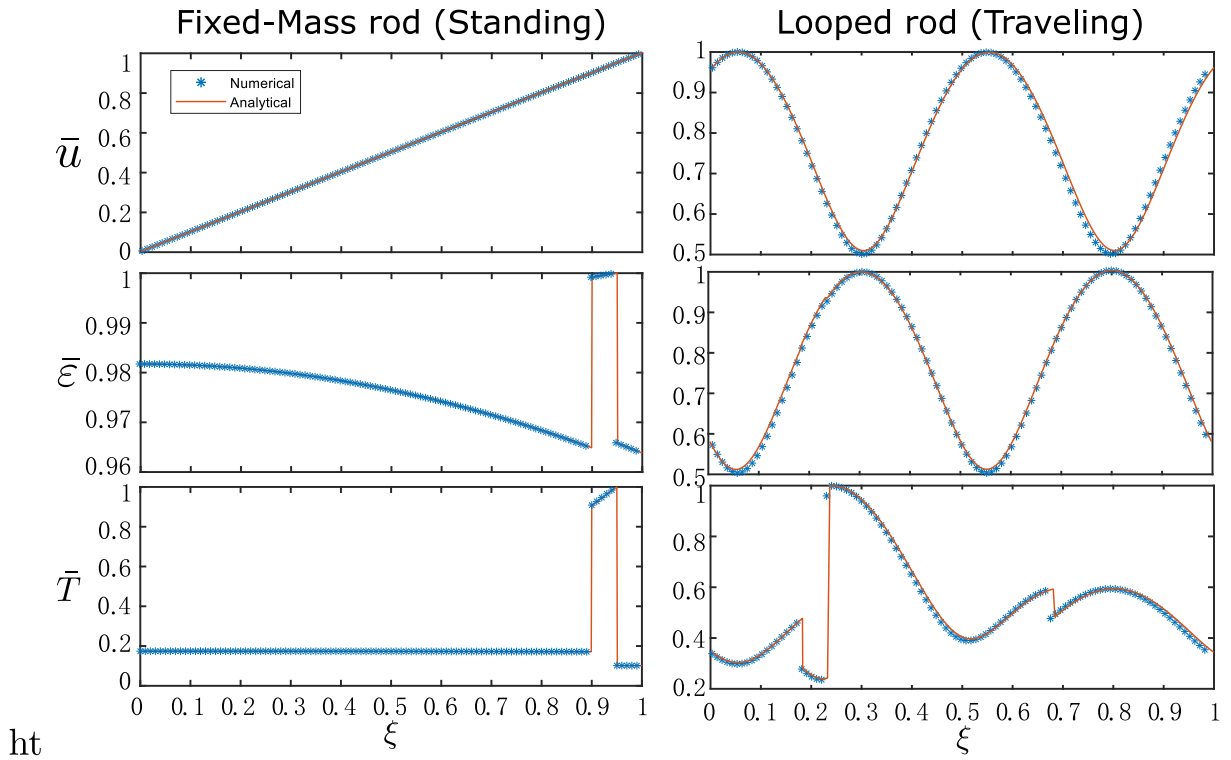

Fig. 3. Mode shapes of displacement, strain, and temperature (normalized by their own maximum value) obtained from both the numerical solver and the analytical approach.

4. Dimensionless parametric analysis

By deriving the dimensionless expressions for the governing equations and boundary conditions (see Eqns. (13)–(19)), it is understood that the growth-to-frequency ratio β/ω is determined by the following dimensionless parameters (divided into four groups):

1. Stage parameters: Temperature ratio, Θ and dimensionless stage location parameter, ξ_h and ξ_c
2. Material parameters: Dimensionless CTE, A and Grüneisen parameter, γ_G
3. Heat-transfer parameter: Dimensionless radius, r
4. Unique parameters
   (a) **Fixed-mass rod:** Mass ratio, m
   (b) **Looped rod:** Thermal buffer segment (TBS) end position ξ_b

Table 6
Reference cases of parametric analysis.

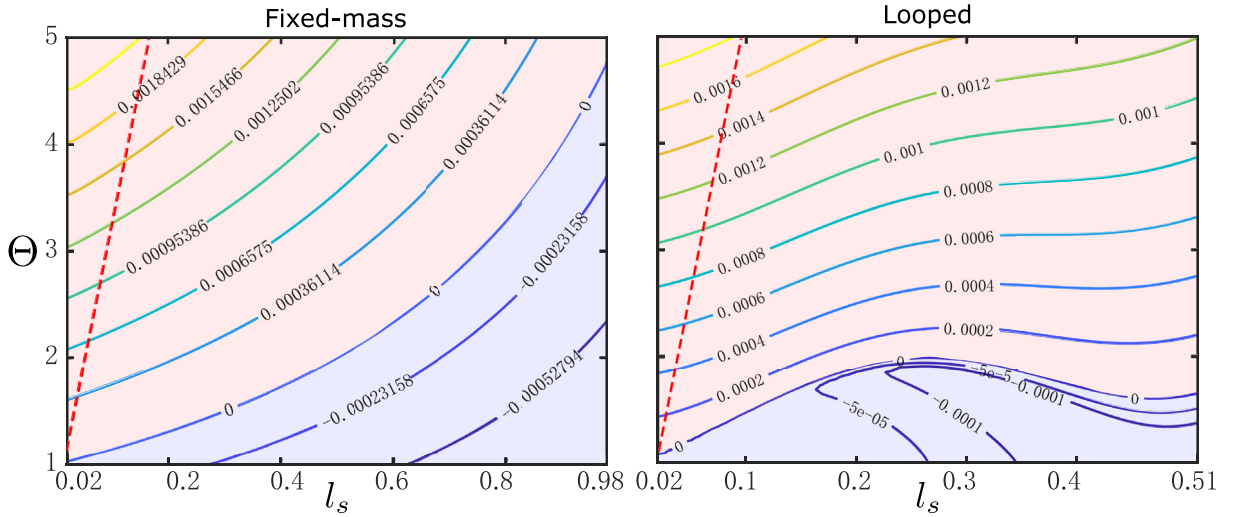| General:	$A = 6.74 \times 10^{-3}$	$\gamma_G = 0.6626$	$\Theta = 1.682$	
Fixed-mass rod:	$r = 3.80\sqrt{1/\omega}$	$\xi_h = 0.9$	$\xi_c = 0.95$	$m = 23.101$
Looped rod:	$r = 0.38\sqrt{1/\omega}$	$\xi_c = 0.02$	$\xi_h = 0.07$	$\xi_b = 0.52$

Fig. 4. Contour plots of the growth ratio β/ω on the $\Theta - l_s$ plane. The whole plane is divided into the stable (blue) and unstable (pink) regions by the $\beta/\omega = 0$ level, indicating the onset of TA instability. The red dashed line represents an isoline of the stage temperature gradient, illustrating the difference of β/ω on the same level of temperature gradient. (For interpretation of the references to colour in this figure legend, the reader is referred to the Web version of this article.)

This section focuses on the analysis regarding the above four groups of parameters and on their effects with regard to the optimization of the growth ratio β/ω. The parameters tabulated in Table 6 are chosen as references for **Fixed-mass rod** and **Looped rod** configurations.

Note that during the parametric analysis, when one group of parameters is varied the remaining are kept constant. This approach helps isolating the effect of a specific set of parameters on β/ω.

4.1. The effect of stage parameters

It is well known that the temperature difference is the key element to determine the onset of TA instability. In the field of fluid thermoacoustics, the stack design is crucial to the efficiency of TAEs [16,17]. For an ideal SSTA engine, the stage (equivalent to a one-pore stack in fluids) has infinite heat capacity, hence it is capable of both suppressing the temperature fluctuation on the surface of the stage segment (Segment 2 for both configurations) and sustaining the spatial temperature gradient. It is intuitive that a larger temperature difference causes a higher growth rate. A quantitative analysis conducted in this section is in line with the intuition. The three parameters in the first group determine the strength of the temperature difference, by Θ, and the location and length of the stage, by ξ_h and ξ_c. In a previous study, Hao et al. [9] pointed out that for a standing wave configuration, the optimal stage location $\xi_s = (\xi_c + \xi_h)/2$ is at 1/8 wavelength from the hot fixed end. This observation was consistent with the conclusions drawn in fluid TA devices [13].[1] For a fixed-mass rod with heavy end mass, the rod length is smaller than 1/8 wavelength, so the optimal location for the stage is at the rod's extremity $\xi = 1 - l_s/2$, where $l_s = |\xi_c - \xi_h|$ is the dimensionless stage length. However, in order to focus on the effect of the stage length l_s and the temperature ratio Θ on growth ratio, the stage location was fixed at the midpoint of the rod $\xi_s = 0.5$ (although not the optimal location).

Differently from the standing wave configuration, the stage location is irrelevant for the looped rod due to its periodicity. Therefore, ξ_c is fixed at 0.02 (close to the left boundary) so to get a larger span of l_s by varying ξ_h. Note that ξ_h cannot exceed $(1 - l_b + \xi_c)$, where $l_b = \xi_b - \xi_h$ is the length of TBS; $l_b = 0.45$ is taken. Fig. 4 shows the growth ratio contours for different temperature ratios Θ and stage lengths l_s. The transition from stable (blue) to unstable (pink) regions is very evident. For a fixed stage length, a stronger temperature difference gives rise to a higher growth ratio, which is consistent with the phenomena observed in fluid TAEs. The red dashed line represents an isoline of temperature gradient $[(\Theta - 1)/l_s]$. It reveals that for stages with same temperature gradient, those providing higher temperature difference, although longer, generate higher growth ratios.

---

[1] In Ref. [13], the optimal stage location for the first mode of a closed-closed tube is 1/4 length away from the hot end. 1/4 tube length for a half-wavelength tube is 1/8 wavelength.
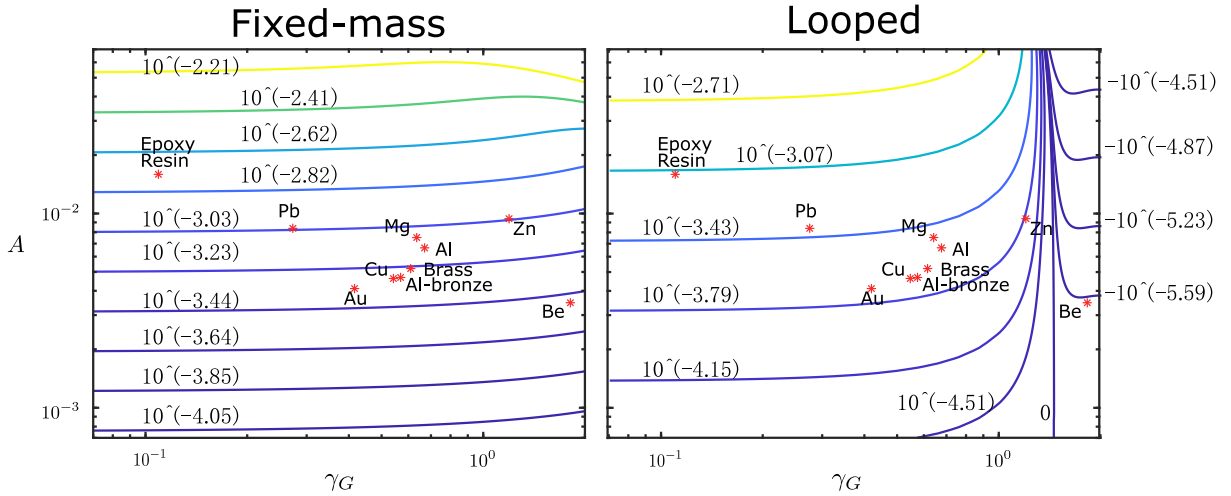
Fig. 5. Contour plots of β/ω on $A - \gamma_G$ plane. The scatters denote the corresponding metals on the plane.

This results illustrate that increasing the temperature difference is generally more effective than shortening the stage. From Fig. 4, another noteworthy observation is that for a short stage (small l_s), the SSTA engine becomes unstable as long as it has a non-zero temperature difference. This result is explained by the fact that the ideal SSTA engine analyzed in this study has zero structural damping, which is the main mechanism of dissipation in solids. In the presence of damping, the critical temperature shall be larger. For a practical design in which damping is present, the multi-stage configuration proposed in Ref. [9] is capable of lowering the onset temperature.

4.2. The effect of material parameters

Compared to fluids, properties of solids can be more easily engineered. Many areas of research including composites, smart materials, and metamaterials have explored several avenues to achieve material properties not readily available in natural materials. Examples include, to name a few, negative density [18], negative stiffness [19], and negative, zero, or colossal CTE [20]. Realistically, one can envision these properties to play a key role in the development of SSTA engines characterized by ultra high efficiency and more versatility in the application spectrum. Therefore, understanding the effect of material properties on TA performance is a crucial step for their development.

From the dimensionless governing equations (Eqns. (13)–(15)), the two material-related parameters left in the equations are the dimensionless CTE $A = \alpha T_c$, and the Grüneisen parameter $\gamma_G = \alpha E/(\rho c_\varepsilon)$. Fig. 5 presents the contour plots of the growth ratio β/ω on $A - \gamma_G$ plane. The markers indicate where some typical solid materials would fall on this plane. The reference case ($A = 6.74 \times 10^{-3}, \gamma_G = 0.6626$) corresponds to Aluminum. The contour plots reveal that for the fixed-mass rod, the growth ratio is always positive and weakly dependent on γ_G (at least, in the chosen range). The growth ratio increases with A. On the contrary, for the looped rod, this same behavior occurs only when $\gamma_G < 1.5$, although most of the showcased materials are located in this region. Beyond $\gamma_G \approx 1.5$, for a given A, the growth ratio decreases rapidly with γ_G increasing and eventually becomes negative. Note that γ_G is the coefficient in front of the thermoelastic coupling term in Eqn. (3). This term acts in the energy equation as a source caused by the irreversible entropy increase due to stress inhomogeneity. The same term acts, in the momentum equation, as a dissipating term that is well-known as thermoelastic damping [21,22].[2] As a result, the increase of γ_G can amplify thermoelastic damping which eventually makes the overall growth rate null or, even, negative. To enhance the TA performance, those materials with high CTE and low γ_G are preferred. Generally, a high CTE is accompanied with low Young's modulus. This behavior is due to the fact that high CTE is due to loose chemical bonds that ultimately prevent high modulus. As a result, a material with high CTE usually has low or moderate γ_G (e.g. epoxy resin). More discussions regarding material properties are presented in Section 5.

4.3. The effect of heat-transfer parameter

The onset of TA instability is a result of energy conversion from heat to mechanical oscillations. The transverse heat transfer taking place underneath the stage plays a crucial role for the performance of TAEs. The ratio of the rod radius R to the thermal

---

[2] From an energy perspective, the decrease in kinetic energy leads to a very slow rise in mean temperature T_0. However, in this study, temperature fluctuation is the variable and the slow variation in T_0 is neglected.
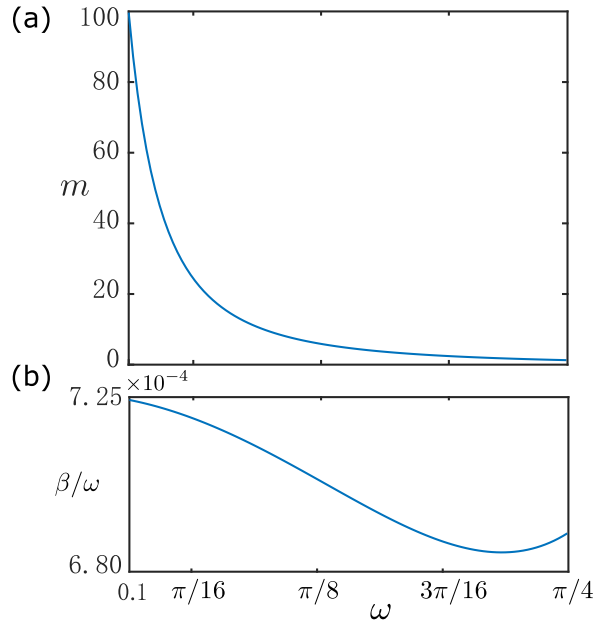
Fig. 6. (a) The relation between mass ratio and dimensionless frequency. (b) Plot of growth ratio for different frequencies induced by variation of mass ratio.

penetration depth δ_k is a metric for thermal coupling that has significant effects on the growth ratio. It has been shown in earlier work that $r = R/\delta_k \approx 2$ is an optimal value for standing wave SSTA systems (Fig. 3(b) in Ref. [9] and Fig. 3 in Ref. [10]). For traveling wave configurations, as $r < 1$, the growth ratio β/ω converges to a value where the traveling wave mode dominates the motion (Fig. 3 in Ref. [10]). In general, a rod with very low radius-to-length aspect ratio is avoided so to prevent the rod being dominated by flexural mode. Therefore, to pursue a larger R while keeping the optimal value of r, a larger δ_k is required as well. The thermal penetration depth is expressed as $\delta_k = \sqrt{2k/\Omega}$, where k is thermal diffusivity. Thus, a material with higher thermal diffusivity is preferred in practical sense. δ_k is a frequency-dependent parameter as well, so for structures with different fundamental frequency, which is affected by rod length and end mass, the radius R should be adjusted accordingly in order to achieve optimal performance.

4.4. The effect of unique parameters

This subsection focuses on the discussion of parameters that are unique to each configuration. They are the mass ratio m for the fixed-mass rod and the TBS end location ξ_b for the looped rod.

4.4.1. Fixed-mass rod: mass ratio

For the dimensionless representation of the fixed-mass rod, the mass ratio m is the only parameter which controls the fundamental frequency, given the negligible effect of thermal coupling and structural damping on frequency. To study the effect of the tip mass, the impact of the heat transfer coefficient is isolated by choosing $r = 2$ (corresponding to the optimal radius value for performance). Fig. 6(a) shows the relation between the mass ratio m and the dimensionless frequency ω. Fig. 6(b) exhibits the change of growth ratio β/ω with frequency ω. In the range of $\omega \in [0.1, \pi/4]$, the value of β/ω varies within $\pm 3\%$ compared to the average in the frequency range. Therefore, we conclude that the dependency of growth ratio on frequency is weak when both the radius and the stage location are selected at their optimal values. It is noteworthy that, in practical designs, a low frequency is still preferable in order to avoid small values of both $\delta_k \propto 1/\sqrt{\omega}$ and R for optimal performance.

The lower limit of ω is chosen as 0.1, since the corresponding mass ratio $m = 100$ is high enough for practical designs. The upper limit $\pi/4$ is to keep the mass end as the optimal stage location for all the values of ω within the range. The frequency is related to the (dimensionless) wavelength λ_w of the rod by $\lambda_w = 2\pi/\omega$. The wavelength determines the optimal location of the stage by $\min[1, \lambda_w/8]$, which has impacts on β/ω, as seen in Ref. [9]. In order to perform a meaningful comparison with the reference, the maximum value of ω was chosen as $\pi/4$, corresponding to $\lambda_w = 8$, the shortest wavelength which makes the mass end the optimal location for stage. To adapt to the 3-segment division of the rod developed for the analytical approach, we set the stage at [0.900.95], same as the reference case, which is not the exact optimal location (extremity) but sufficiently close. For all the values of ω under consideration, this location is regarded the optimal. Hence, in the frequency range $\omega \in [0.1, \pi/4]$, fixing the stage at [0.900.95] excludes the effect of stage location on β/ω. The variation of β/ω is shown in Fig. 6(b) and it is exclusively due to the effect of the frequency.
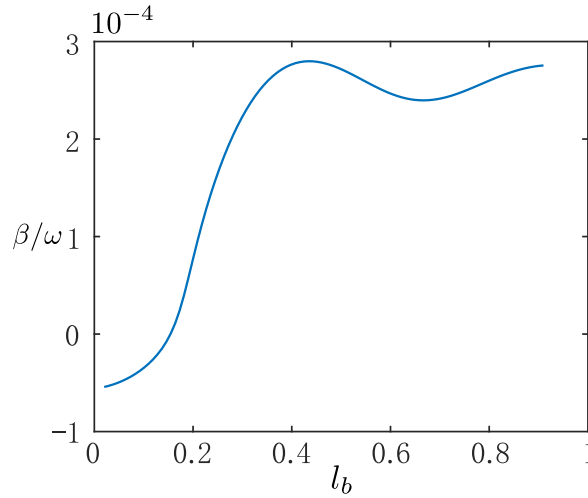
Fig. 7. The plot of β/ω vs. l_b.

4.4.2. Looped rod: TBS length

Fig. 7 plots the growth ratio β/ω versus the TBS length l_s of the looped rod. It is seen that the optimal TBS length is $l_b = 0.45$. This is consistent with the conclusion drawn in Ref. [10], Fig. S1.

5. Discussions

Section 4.2 revealed that in the "γ_G-independent" region, a larger CTE is preferable for both standing- and traveling-wave configurations. Polymers generally have one-order-of-magnitude larger CTE compared to metals. The epoxy resin (see Fig. 5), as an example, causes higher growth ratio according to the prediction of the lossless linear SSTA theory. However, the high viscous loss in polymers is unfavorable for SSTA devices. Besides, the applicability of the linear theory for polymers is reduced very quickly due to their nonlinear viscoelastic behavior enhanced by large amplitude oscillations. So, unless considering engineered polymers, it is not likely that polymers could provide better performance for SSTA devices.

Another promising type of cellular solid is made of curved bimetallic ribs with void spaces. This two-dimensional material, first proposed by Lakes [20], can exhibit tunable and colossal CTE. A three-dimensional lattice was also envisioned in a follow-up work [23] by Lakes. Experiments on 3D fabricated prototypes of highly tunable CTE structures have been conducted by Xu and Pasini [24]. The CTE of such a structure is given by:

$$\alpha = \frac{l_{arc}}{t}\left(\alpha_1 - \alpha_2\right)\frac{\varphi}{12} \tag{68}$$

where l_{arc}, t, and φ are the arc length, thickness, and angle of the bimetallic rib, while α_1 and α_2 are the CTE for the two layers. By making the ribs more slender (a smaller aspect ratio t/l_{arc}), the magnitude of α can become unbounded. While exhibiting high CTE, the dissipation of such structure shall be in the same order of bulk metals. In addition, the voids inside the structure reduce the density ρ and the specific heat c_ε, although they cause lower thermal conductivity κ as well. Lower ρ and c_ε might lead to higher thermal penetration depth δ_k, which is favorable for practical designs.

According to Eqn. (68), the effective CTE can be made negative if $\alpha_1 < \alpha_2$, which physically means that the layer with higher CTE is on the convex side. The negative CTE is a unique property for solids. Negative-CTE materials can be potentially applied in SSTA engines.

We first numerically prove that a negative-CTE material accompanied with an inverse temperature gradient can produce SSTA instability as well. Fig. 8 shows the comparison between a regular SSTA configuration (reference) and one with inverse temperature gradient and negative CTE of the same magnitude. The growth ratio for the latter configuration is also positive and quite close to the reference case.

The negative-CTE material accompanied by the inverse temperature gradient can be applied to the multi-stage configuration proposed in Ref. [9]. As the distance between adjacent stages is reduced, the natural conduction between them might become problematic leading to the reduction of the temperature difference in each stage (see red line in Fig. 9(a)). As an alternative, a new configuration with staggered stages (see Fig. 9(b)) could be envisioned. The direction of the temperature gradient of adjacent stages (being opposite to each other) avoids the natural conduction between stages. However, in this configuration, the segment underneath the inverse temperature gradient needs to have negative CTE to make positive contributions to the TA process. In order to explore the performance of these concepts, the two configurations were numerically simulated using a commercial finite element software (COMSOL Multiphysics). Thirty stages with 250 K temperature difference were distributed along an aluminum rod with 1.8 m length and 1 mm radius. One end of the rod was fixed, while a 0.3527 kg mass was attached

Fig. 8. Comparison between the reference case (left column) and its counterpart with negative CTE of same magnitude and inverse temperature gradient (right column). Both induce TA instability with an approximately equivalent growth ratio. To keep the notation consistent with the analytical approach, in the "Negative CTE" case, T_c and T_h still correspond to the temperature for Segment 1 and Segment 3, respectively, although in this case T_c is higher than T_h.

to the other end. The negative CTE was chosen to be -23×10^{-6} [1/K] for case (b). Fig. 9(c) and (d) show the displacement at the mass end in configuration (a) and (b). The non-zero mean is due to the static thermal expansion of the rod. In case (b), the contraction effects due to the negative-CTE segments cancel part of the expansion from other segments. As a result, the mean thermal deformation is smaller than that in case (a). Note that in case (b), while the CTE was chosen to be a negative value, the other parameters were kept consistent with those of aluminum. In reality, a hollow structure has lower effective density, specific heat, and Young's modulus, so more elaborate modeling considerations should be employed to properly account for
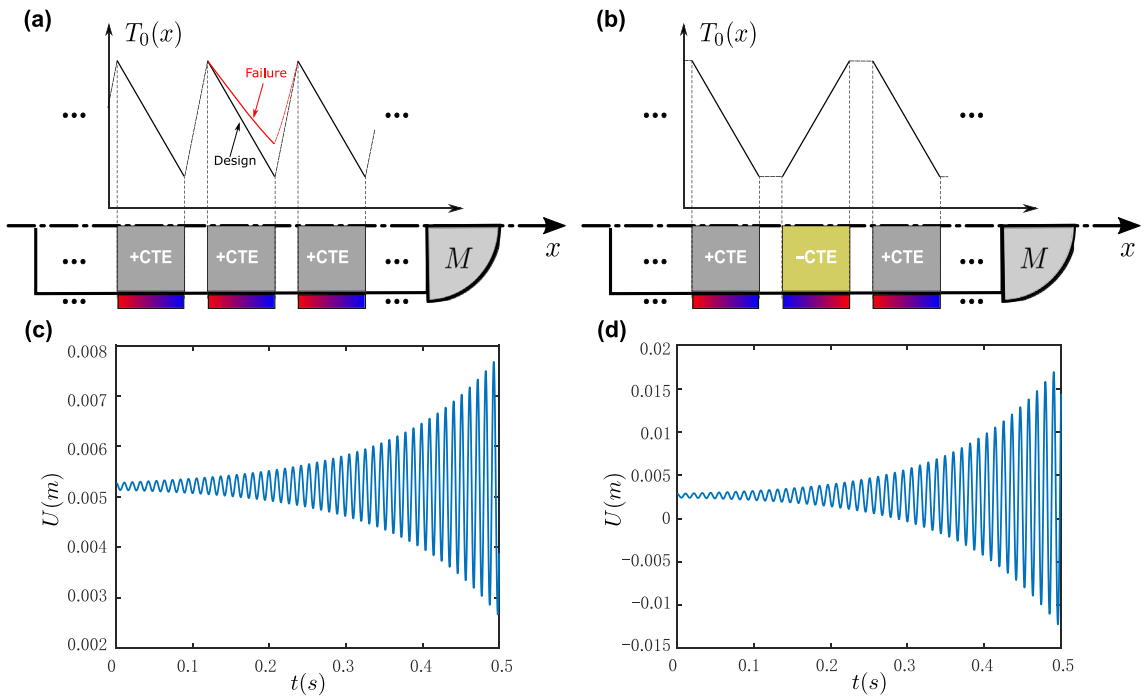

Fig. 9. (a) Multi-stage configuration proposed in Ref. [9]. Natural conduction in between stages might be detrimental to performance if the separation is small. (b) Staggered multi-stage design with segments alternating positive and negative CTE as well as the temperature gradient profile. In this configuration, the temperature at the two ends of adjacent stages is identical, hence no natural conduction takes place. (c) Displacement at the mass end in case (a). (d) Displacement at the mass end in case (b).

effective properties of materials. Nevertheless, Fig. 9(b) shows that a staggered multi-stage configuration by use of negative-CTE materials is plausible and could yield more robust SSTA devices.

6. Conclusion

In this study, we have presented contributions that impact the science of SSTA at three different levels.

(1) A dimensionless form of the governing equations for SSTA responses of a fixed-mass rod and a looped rod is derived and analytical approaches to solve them are proposed. Although the analytical solutions are not amenable to closed form, they provide valuable information on the form of mode shapes, and lay the foundation for the dimensionless parametric study. (2) The analysis regarding the dimensionless parameters reveals the dependence of the growth ratio on the stage design, the rod radius (wall heat transfer), the material properties, and the parameters unique to each configuration. (3) Possible design configurations enlightened by the parametric study are envisioned, and some preliminary results are provided. More specific conclusions for the enhancement of SSTA performance are summarized in the following:

1. The ratio of rod radius R to thermal penetration depth δ_k, which is dependent on frequency, is a metric for thermal coupling. For a standing wave configuration, $R/\delta_k \approx 2$ is optimal [9,10].
2. For a given stage length, there exists a critical temperature difference which triggers the onset of TA instability. The higher the temperature difference, the stronger the TA response. For a same level of temperature gradient, higher temperature difference is favorable.
3. For fixed-mass rods, the mass ratio m affects the operating frequency ω. In the range $\omega \in [0.1, \pi/4]$, where the mass end is kept at the optimal location, the growth ratio β/ω only varies 3% with frequency ω.
4. Unlike the thermal buffer tube in fluid-based thermoacoustic devices, the TBS in SSTA engines is not expected to yield wave-scattering effect, due to the negligible temperature dependency of sound speed [10]. However, for looped rods, there does exist an optional length of the TBS. For the configuration studied in this paper (an aluminum looped rod under 200 K temperature difference over a 5%L stage), the optimal TBS length is 0.45L.
5. Large CTE materials are favorable for SSTA instability. However, polymers, having CTE one order of magnitude larger than metals, are highly dissipative due to their nonlinear viscoelastic nature. More comprehensive analyses leveraging a nonlinear formulation would be needed in order to determine the feasibility of the use of polymers for SSTA devices.
6. Engineering structures involving curved bimetallic ribs with voids can exhibit positive or negative CTE with unbounded magnitude. Hollow micro-scale structures with high CTE could be a good choice for SSTA devices due to their low dissipation and low density and specific heat. Negative-CTE segments allow the application of inverse temperature gradient, which can be used in multi-stage configurations. A staggered multi-stage SSTA design is proposed in this study. By elaborating the staggered distribution of positive- and negative-CTE segments (Fig. 8(b)), the detrimental effect due to the natural conduction between adjacent stages can be eliminated.

The parametric analyses conducted in this work provide new insights on the selection and design of materials for the optimization of SSTA devices. The authors envision that with the unique properties of solid-based engineered materials, robust SSTA devices can provide a wider range of applications than their fluid counterparts.

Author contributions section

Hao conceived the original idea, derived the analytical approaches and conducted the parametric study. Semperlotti and Scalo supervised the project. All authors analyzed and discussed the results; and contributed to the final manuscript.

Appendix A. Matrix $\underline{C}$ in Case 2 (Looped rod)

The elements of $\underline{C}$ are given by:

$$\underline{C}(1,1) = e^{i\lambda R_3 \xi_c}, \quad \underline{C}(1,2) = e^{-i\lambda R_3 \xi_c}$$

$$\underline{C}(1,3) = 1 + \sum_{n=2}^{\infty} \xi_c^n d_{\varphi 0}(n), \quad \underline{C}(1,4) = \xi_c + \sum_{n=2}^{\infty} \xi_c^n d_{\varphi 1}(n)$$

$$\underline{C}(2,1) = \left[(1 + A\gamma_G)(i\lambda R_3) - \frac{A}{1 - g_k} \frac{\Theta - 1}{\xi_h - \xi_c} \right] e^{i\lambda R_3 \xi_c}$$

$$\underline{C}(2,2) = -\left[(1 + A\gamma_G)(i\lambda R_3) + \frac{A}{1 - g_k} \frac{\Theta - 1}{\xi_h - \xi_c} \right] e^{-i\lambda R_3 \xi_C}$$

$$\underline{C}(2,3) = -\left(1 + \frac{A\gamma_G}{1 - g_k} \right) \sum_{n=2}^{\infty} n\xi_c^{n-1} d_{\varphi 0}(n)$$

$$\underline{C}(2,4) = -\left(1 + \frac{A\gamma_G}{1-g_k}\right)\sum_{n=2}^{\infty} n\xi_c^{n-1} d_{\varphi 1}(n)$$

$$\underline{C}(3,3) = 1 + \sum_{n=2}^{\infty} \xi_h^n d_{\varphi 0}(n), \quad \underline{C}(3,4) = \xi_h + \sum_{n=2}^{\infty} \xi_h^n d_{\varphi 1}(n)$$

$$\underline{C}(3,5) = 1 + \sum_{n=2}^{\infty} \xi_h^n d_{\psi 0}(n), \quad \underline{C}(3,6) = \xi_h + \sum_{n=2}^{\infty} \xi_h^n d_{\psi 1}(n)$$

$$\underline{C}(4,3) = \left(1 + \frac{A\gamma_G\Theta}{1-g_k}\right)\sum_{n=2}^{\infty} n\xi_h^{n-1} d_{\varphi 0}(n) + \frac{A}{1-g_k}\frac{\Theta-1}{\xi_h-\xi_c}\left(1 + \sum_{n=2}^{\infty} \xi_h^n d_{\varphi 0}(n)\right)$$

$$\underline{C}(4,4) = \left(1 + \frac{A\gamma_G\Theta}{1-g_k}\right)\sum_{n=2}^{\infty} n\xi_h^{n-1} d_{\varphi 1}(n) + \frac{A}{1-g_k}\frac{\Theta-1}{\xi_h-\xi_c}\left(1 + \sum_{n=2}^{\infty} \xi_h^n d_{\varphi 1}(n)\right)$$

$$\underline{C}(4,5) = -\left(1 + A\gamma_G\Theta\right)\sum_{n=2}^{\infty} n\xi_h^{n-1} d_{\psi 0}(n) - A\frac{\Theta-1}{\xi_h-\xi_b}\left(1 + \sum_{n=2}^{\infty} \xi_h^n d_{\psi 0}(n)\right)$$

$$\underline{C}(4,6) = -\left(1 + A\gamma_G\Theta\right)\sum_{n=2}^{\infty} n\xi_h^{n-1} d_{\psi 1}(n) - A\frac{\Theta-1}{\xi_h-\xi_b}\left(1 + \sum_{n=2}^{\infty} \xi_h^n d_{\psi 1}(n)\right)$$

$$\underline{C}(5,1) = -e^{i\lambda R_3(\xi_b-1)}, \quad \underline{C}(5,2) = -e^{-i\lambda R_3(\xi_b-1)}$$

$$\underline{C}(5,5) = 1 + \sum_{n=2}^{\infty} \xi_b^n d_{\psi 0}(n), \quad \underline{C}(5,6) = \xi_b + \sum_{n=2}^{\infty} \xi_b^n d_{\psi 1}(n)$$

$$\underline{C}(6,1) = \left[A\frac{\Theta-1}{\xi_h-\xi_b} - (1 + A\gamma_G)(1i\lambda R_3)\right]e^{i\lambda R_3(\xi_b-1)}$$

$$\underline{C}(6,2) = \left[A\frac{\Theta-1}{\xi_h-\xi_b} + (1 + A\gamma_G)(1i\lambda R_3)\right]e^{-i\lambda R_3(\xi_b-1)}$$

$$\underline{C}(6,5) = \left(1 + A\gamma_G\right)\sum_{n=2}^{\infty} n\xi_b^{n-1} d_{\psi 0}(n) \quad \underline{C}(6,6) = (1 + A\gamma_G)\sum_{n=2}^{\infty} n\xi_b^{n-1} d_{\psi 1}(n)$$

The elements in $\underline{C}$ that were not defined above are implicitly assumed equal to zero.

References

[1] T. Poinsot, D. Veynante, Theoretical and Numerical Combustion, R. T. Edwards, 2011. Inc., Philadelphia, PA.
[2] J.L. Rayleigh, The explanation of certain acoustical phenomena, Nature 18 (1878) 319–321, https://doi.org/10.1038/018319a0.
[3] G. Swift, Thermoacoustic engines, J. Acoust. Soc. Am. 84 (4) (1998) 1145–1180, https://doi.org/10.1121/1.396617.
[4] C. Scalo, S. Lele, L. Hesselink, Linear and nonlinear modelling of a theoretical travelling-wave thermoacoustic heat engine, J. Fluid Mech. 766 (2015) 368–404, https://doi.org/10.1017/jfm.2014.745.
[5] G. Chen, L. Tang, B. Mace, Theoretical and experimental investigation of the dynamic behaviour of a standing-wave thermoacoustic engine with various boundary conditions, Int. J. Heat Mass Transf. 123 (2018) 367–381, https://doi.org/10.1016/j.ijheatmasstransfer.2018.02.121.
[6] P. Rijke, LXXI. Notice of a new method of causing a vibration of the air contained in a tube open at both ends, Philos. Mag. Ser. 17 (116) (1859) 419–422, https://doi.org/10.1080/14786445908642701.
[7] G. Chen, L. Tang, B.R. Mace, Modelling and analysis of a thermoacoustic-piezoelectric energy harvester, Appl. Therm. Eng. 150 (2019) 532–544, https://doi.org/10.1016/j.applthermaleng.2019.01.025.
[8] N. Rott, Damped and thermally driven acoustic oscillations in wide and narrow tubes, Z. Angew. Math. Phys. 20 (2) (1969) 230–243, https://doi.org/10.1007/BF01595562.
[9] H. Hao, C. Scalo, M. Sen, F. Semperlotti, Thermoacoustics of solids: a pathway to solid state engines and refrigerators, J. Appl. Phys. 123 (2) (2018) 024903 https://doi.org/10.1063/1.5006489.
[10] H. Hao, C. Scalo, M. Sen, F. Semperlotti, Traveling and standing thermoacoustic waves in solid media, J. Sound Vib. 449 (2019) 30–42, https://doi.org/10.1016/j.jsv.2019.02.029.
[11] S. Cummer, J. Christensen, A. Alu, Controlling sound with acoustic metamaterials, Nat. Rev. Mater. 1 (3) (2016) 16001, https://doi.org/10.1038/natrevmats.2016.1.
[12] G. Ma, P. Sheng, Acoustic metamaterials: From local resonances to broad horizons, Sci. Adv. 2 (2) (2016), https://10.1126/sciadv.1501595.
[13] M. Guedra, G. Penelet, On the use of a complex frequency for the description of thermoacoustic engines, Acta Acustica United Acustica 98 (2) (2012) 232–241, https://doi.org/10.3813/AAA.918508.
[14] B. Yates, Thermal Expansion, Plenum Press, New York, NY, 1972.
[15] H. Hao, C. Scalo, M. Sen, F. Semperlotti, Solid-state thermoacoustics, in: INTER-NOISE 2018 - 47th International Congress and Exposition on Noise Control Engineering: Impact of Noise Control Engineering, vol. 258, 2018, pp. 432–439.
[16] A. Trapp, F. Zink, O. Prokopyev, L. Schaefer, Thermoacoustic heat engine modeling and design optimization, Appl. Therm. Eng. 31 (1415) (2011) 2518–2528, https://doi.org/10.1016/j.applthermaleng.2011.04.017.
[17] M. Tijani, J. Zeegers, Design of thermoacoustic refrigerators, Cryogenics 42 (1) (2002) 49–57, https://doi.org/10.1016/S0011-2275(01)00179-5.

[18] H.H. Huang, C.T. Sun, G.L. Huang, On the negative effective mass density in acoustic metamaterials, Int. J. Eng. Sci. 47 (4) (2009) 610–617, https://doi.org/10.1016/j.ijengsci.2008.12.007.

[19] R.S. Lakes, T. Lee, A. Bersie, Y.C. Wang, Extreme damping in composite materials with negative-stiffness inclusions, Nature 410 (6828) (2001) 565–567, https://doi.org/10.1038/35069035.

[20] R. Lakes, Cellular solid structures with unbounded thermal expansion, J. Mater. Sci. Lett. 15 (6) (1996) 475–477, https://doi.org/10.1007/BF00275406.

[21] C. Zener, Internal friction in solids II. General theory of thermoelastic internal friction, Phys. Rev. 53 (1938) 90–99, https://doi.org/10.1103/PhysRev.53.90.

[22] M. Biot, Thermoelasticity and irreversible thermodynamics, J. Appl. Phys. 27 (3) (1956/03) 240–253, https://doi.org/10.1063/1.1722351.

[23] R. Lakes, Cellular solids with tunable positive or negative thermal expansion of unbounded magnitude, Appl. Phys. Lett. 90 (22) (2007) 221905 https://doi.org/10.1063/1.2743951.

[24] H. Xu, D. Pasini, Structurally efficient three-dimensional metamaterials with controllable thermal expansion, Sci. Rep. 6 (1) (2016), https://doi.org/10.1038/srep34924.